Physics of Fluids

Collision integrals for $N(^4S)$–$N(^4S)$, $N(^4S)$–$N(^2D)$, and $N(^4S)$–$N(^2P)$ interactions

Cite as: Phys. Fluids **35**, 027127 (2023); https://doi.org/10.1063/5.0136416
Submitted: 25 November 2022 • Accepted: 04 February 2023 • Accepted Manuscript Online: 06 February 2023 • Published Online: 23 February 2023

Zi Ding (丁子), **Zhi Qin** (秦智) and **Linhua Liu** (刘林华)

Physics of Fluids ARTICLE scitation.org/journal/phf

Collision integrals for N(^{4}S)–N(^{4}S), N(^{4}S)–N(^{2}D), and N(^{4}S)–N(^{2}P) interactions

Cite as: Phys. Fluids **35**, 027127 (2023); doi: 10.1063/5.0136416
Submitted: 25 November 2022 · Accepted: 4 February 2023 ·
Published Online: 23 February 2023

Zi Ding (丁子),[1,2] Zhi Qin (秦智),[1,2,a)] and Linhua Liu (刘林华)[1,2,3,a)]

AFFILIATIONS

[1]Optics & Thermal Radiation Research Center, Institute of Frontier and Interdisciplinary Science, Shandong University, Qingdao 266237, China
[2]School of Energy and Power Engineering, Shandong University, Jinan 250061, China
[3]School of Energy Science and Engineering, Harbin Institute of Technology, Harbin 150001, China

Note: This paper is part of the special topic, Hypersonic Flow.
[a)]**Authors to whom correspondence should be addressed:** z.qin@sdu.edu.cn and liulinhua@sdu.edu.cn

ABSTRACT

Collision integrals for the scattering of nitrogen (N) atoms are essential to model transport properties of air plasmas, which can be highly dependent on the species involved. At high temperatures, N atoms may exist in their excited states. Therefore, collision integrals for N atoms are computed at the temperature range of 500–50 000 K, in which the interactions between the excited [N(^{2}D) and N(^{2}P)] atoms and ground N(^{4}S) atom are considered. The interaction between the excited N(^{2}P) atom and ground N(^{4}S) atom is considered for the first time. A comparison of the collision integrals from our combined-hyperbolic-inverse-power-representation (CHIPR) potential energy function with those obtained using other analytical potential energy functions in the literature is given. The results show that the trend of potential energy curves (PECs) in dissociated asymptotic and short-range regions has an important effect on the collision integrals. These regions are difficult to cover in experiments. Here we seek the state-of-the-art *ab initio* methods for a theoretical guideline to compute the PECs of N_2, which are then modeled by the CHIPR function. PECs of some low-lying states are also refined by available experimental spectroscopic data. Overall, our collision integrals are reliable.

I. INTRODUCTION

High-temperature plasma plays an essential role in the fields of machining, metallurgy, chemical production, material preparation, environmental protection, aerospace and space exploration.[1–7] Especially, in the hypersonic flight, when a vehicle moves through the Earth's atmosphere at high supersonic speeds, high-temperature plasmas produce in the front of the vehicle, in which a series of complex physicochemical processes, such as the excitation of energy level, dissociation, recombination, ionization, and photochemistry for the involved species, take place.[8] These physicochemical reactions are usually accompanied by the energy conversion between thermal energy and chemical energy, which can further modify the structure and transport characteristics of high-temperature plasmas.[9–12] Also, calculations of transport properties, such as viscosity coefficients, diffusion coefficients, thermal conductivity, and electrical conductivity, rely on collision integrals.[13,14] Therefore, high-accuracy collision integrals are needed for the reliable calculation of transport properties.

Levin *et al.*[15] calculated the collision integrals of N_2 using *ab initio* data and experimental spectroscopic data at 250–100 000 K. Capitelli *et al.*[16] calculated the collision integrals of air species according to the combination of Lennard–Jones (LJ) and Born–Meyer potentials at 50–100 000 K. Kim *et al.*[17] proposed an elastic collision model for direct simulating the collision integral of N_2 at 2000–100 000 K. Pfeiffer[18] presented a collision-averaged parameter set for the variable soft-sphere collision model and calculated the collision integrals for a range of air mixtures. Hirschfelder *et al.*[19] proposed a simple phenomenological approach for evaluating the transport coefficients for electronically excited atoms, which is further developed by Istomin *et al.*[20,21] The approach is based on the varying atomic diameters of excited electronic states and uses a simple Slater formula for the evaluation of transport coefficients, which is helpful to calculate the collision integral of the excited state. Based on their results, this approach selects the influence factor $f_{\mathrm{int}} = 1.328$ at less than 3000 K and $f_{\mathrm{int}} = 1.42$ at 3000–25 000 K when calculating the transport coefficients in high-temperature flows with electronically

excited species. Buchowiecki *et al.*[22] calculated the collision integrals for the N–N interaction according to the m-6-8 and Hulburt–Hirschfelder (HH) potentials and analyzed the difference between both types of potential function. However, previous studies only focused on the interactions between ground N(^{4}S) atoms. Concerning the interactions between the excited atoms [N(^{2}D) and N(^{2}P)] and ground N(^{4}S) atoms, a few references can be found in the literature.[23,24] In high-temperature plasmas, atoms are easily excited to high electronic states. The interactions between the atomic ground and excited states should not be neglected.

In addition, collision integrals were usually calculated with the analytical potential energy function. Most frequently applied analytical potential energy functions in previous studies include Lennard–Jones (LJ),[25,26] m-6-8, HH,[27–30] Murrell–Sorbie (MS),[31] and Modified Morse (MM)[32] potentials. However, these analytical potential energy functions can accurately produce the potential wells of potential energy curves (PECs), but provide different trends for the dissociated asymptotic and short-range regions, resulting in different results for the collision integrals. Recently, Buchowiecki *et al.*[33] also pointed out that the different trends for the PECs in the short-range region generated different collision integrals at high temperatures. Consequently, accurate PECs are very important in the calculation of collision integrals.

Experimental spectroscopic data can only be used to reproduce potential energy wells of some low-lying electronic states, theoretical techniques are thus needed to give the potential energies in dissociated asymptotic and short-range regions, as well as the whole PECs of high-lying electronic states where experimental spectroscopic data are not available. Over the past few decades, the computational accuracy of *ab initio* methods has improved significantly. Wright *et al.*[34] studied the transport coefficients of the weakly ionized CO_2–N_2 mixture, which exhibited that the accuracy of the results from *ab initio* potential energies is within 5%. In a comparative analysis of thermophysical-properties data and scattering data, Aziz *et al.*[35] demonstrated that the accuracy of transport properties and virial coefficients based on *ab initio* potential energies for helium exceeded the best measurement available at that time, and the results from *ab initio* potential energies can be used for the calibration of the measurements. Consequently, *ab initio* potential energy data can be accepted as a benchmark when experimental spectroscopic data are not available.

Taking above into consideration, the combined-hyperbolic-inverse-power-representation (CHIPR) method[36–39] is used to obtain the PECs in this work, which can not only accurately fit *ab initio* potential energy points but also allow further refinement of PECs using available experimental spectroscopic data. Except for the experimentally refined potential energy wells, this method can accurately fit *ab initio* PECs in the dissociated asymptotic and short-range regions, which can give reliable collision integrals. The primary motivation of this work is to obtain collisional integrals of N(^{4}S)–N(^{4}S), N(^{4}S)–N(^{2}D), and N(^{4}S)–N(^{2}P) interactions by adopting the CHIPR PECs. The collisional integrals between the excited atoms [N(^{2}D) and N(^{2}P)] and ground N(^{4}S) atom are reported for the first time.

The paper is structured as follows. Section II describes the methodology for computing the collision integrals, giving the source of our *ab initio* PECs and the theory of the CHIPR method. Section III discusses the impact of different PECs on the collision integrals. Conclusions are drawn in Sec. IV.

II. METHODOLOGY

A. Calculation of the collision integrals

The deflection angle of scattering atoms interacting with potential energy $V(R)$ is expressed as follows:[40]

$$\chi(b,\gamma) = \pi - 2b\int_{r_c}^{\infty} \mathrm{d}R/\left[R^2\sqrt{1 - b^2/R^2 - V(R)/(kT\gamma^2)}\right], \quad (1)$$

where b is the impact parameter, r_c is the distance of the closest approach, R is the internuclear distance, $\gamma^2 = \mu g^2/(2kT)$, k is Boltzmann constant, T is temperature, μ is reduced mass, and g is relative velocity. Given the deflection angle χ for an impact parameter b, the collision cross section can be obtained by

$$Q^l(\gamma) = 2\pi\int_0^{\infty}\left[1 - \cos^l(b,\gamma)\right] b\mathrm{d}b. \quad (2)$$

Reduced collision integrals $\sigma^2\Omega^{(l,s)*}$ can be expressed as follows:[33,41]

$$\sigma^2\Omega^{(l,s)*} = \frac{4}{(s+1)!\left[1 - \frac{1+(-1)^l}{2(1+l)}\right]}\int_0^{\infty} e^{-\gamma^2}\gamma^{2s+3}Q^l(\gamma)\mathrm{d}\gamma, \quad (3)$$

where (l,s) is the order of the collision integrals. σ is the collision diameter. According to the Withmer–Wigner rule,[42] the interactions of two N atoms can occur along either one of the PECs corresponding to their dissociation limit, and the statistical collision integral is defined as follows:

$$\sigma^2\Omega^{(l,s)*} = \frac{\sum_i w_i\sigma^2\Omega_i^{(l,s)*}}{\sum_i w_i}, \quad (4)$$

where w_i and $\sigma^2\Omega^{(l,s)*}$ are the statistical weight and reduced collision integral associated with every dissociation limit at the ith electronic state, respectively.

B. *Ab initio* calculations of potential energy curves

The triplet states of N_2 were chosen from Qin *et al.*,[43] who used the valence internally contracted multireference configuration-interaction (icMRCI) method with the Davidson correction, as well as the core-valence (CV) correction, scalar relativistic correction, and basis-set extrapolation. Here, we adopted the same treatment as Qin *et al.*[43] to compute the PECs of quintet and septet states for N_2, where MOLPRO 2015 program suite was employed.[44,45] In this work, the aug-cc-pV5Z (AV5Z) and aug-ccpV6Z (AV6Z) basis sets[46–48] were adopted to extrapolate the potential energies (denoted as icMRCI+Q/56). CV correlation energy correction was obtained by the icMRCI approach using the aug-cc-pCV5Z basis set.[46] Scalar relativistic energy correction was calculated via the third-order Douglas–Kroll–Hess (DKH3) Hamiltonian approximation[49–51] at the icMRCI level of theory. The full point group of N_2 is $D_{\infty h}$, which cannot be used directly in MOLPRO. The D_{2h} symmetry, which is the largest Abelian subgroup of the $D_{\infty h}$, was adopted here. The reducing map of irreducible representations from $D_{\infty h}$ to D_{2h} is as follows:

TABLE I. Electronic states of N_2 and their corresponding dissociation limits.

Dissociation limit	Molecular electronic states
$N(^4S)$–$N(^4S)$	$X\ ^1\Sigma_g^+$, $A\ ^3\Sigma_u^+$, $A'\ ^5\Sigma_g^+$, $1\ ^7\Sigma_u^+$
$N(^4S)$–$N(^2D)$	$B\ ^3\Pi_g$, $W\ ^3\Delta_u$, $C\ ^3\Pi_u$, $G\ ^3\Delta_g$, $E\ ^3\Sigma_g^+$, $2\ ^3\Sigma_u^+$, $C''\ ^5\Pi_u$, $2\ ^5\Sigma_g^+$, $1\ ^5\Pi_g$, $1\ ^5\Delta_g$, $1\ ^5\Delta_u$, $1\ ^5\Sigma_u^+$
$N(^4S)$–$N(^2P)$	$B'\ ^3\Sigma_u^-$, $1\ ^3\Sigma_g^-$, $2\ ^3\Pi_u$, $2\ ^3\Pi_g$, $2\ ^5\Pi_u$, $1\ ^5\Sigma_g^-$, $2\ ^5\Pi_g$, $2\ ^5\Sigma_u^-$

$$\begin{aligned} \Sigma_g^+ &\to A_g, & \Sigma_u^+ &\to B_{1u}, \\ \Sigma_g^- &\to B_{1g}, & \Sigma_u^- &\to A_u, \\ \prod_g &\to (B_{2g}, B_{3g}), & \prod_u &\to (B_{3u}, B_{2u}), \\ \Delta_g &\to (A_g, B_{1g}), & \Delta_u &\to (B_{1u}, A_u). \end{aligned} \tag{5}$$

In the calculations, except for the valence molecular orbitals (MOs), we added two more σ_g and two more π_u MOs in the active space for better relaxation of high-lying states. Finally, 1 singlet, 11 triplet, 11 quintet, and 1 septet states are considered, corresponding to the first three dissociation limits. These electronic states are shown in Table I.

To further verify the reliability of our *ab initio* data, the calculated PECs of the $A'\ ^5\Sigma_g^+$ and $C''\ ^5\Pi_u$ states are compared with those from Hochlaf *et al.*[52] and da Silva *et al.*,[53] as shown in Fig. 1. For the $A'\ ^5\Sigma_g^+$ state, our calculations provide a slightly lower PEC than their results. For $C''\ ^5\Pi_u$ state, our PEC is slightly lower than previous data[52,53] for internuclear distances smaller than 2.4 Bohr. In the internuclear range of approximately 2.4–3.3 Bohr, our PEC is lower than those of da Silva *et al.*[53] and essentially coincide with those of Hochlaf *et al.*[52] In addition, our PEC lies between that from Hochlaf *et al.*[52] and that from da Silva *et al.*[53] at internuclear distances beyond 3.3 Bohr. Overall, a reasonable agreement between our PECs of the $A'\ ^5\Sigma_g^+$ and $C''\ ^5\Pi_u$ states and those from previous calculations is observed, thus ensuring the reliability of *ab initio* calculations in this work. Comparisons of our *ab initio* PECs for other electronic states with those from previous calculations are in the supplementary material for brevity.

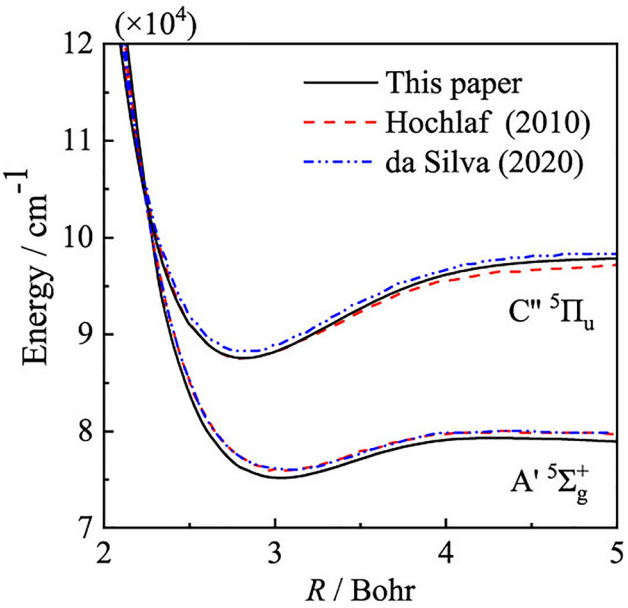

FIG. 1. Comparison of potential energy curves for the $A'\ ^5\Sigma_g^+$ and $C''\ ^5\Pi_u$ states with those from Hochlaf *et al.*[52] and da Silva *et al.*[53]

C. The CHIPR method

When considering the Coulomb interaction, diatomic PECs can be modeled using the CHIPR method,[54,55] given by

$$V(R) = \frac{Z_A Z_B}{R} \sum_{k=1}^{L} C_k y^k, \tag{6}$$

where Z_A and Z_B represent the nuclear charges of atoms A and B, respectively. C_k is the expansion coefficient. y^k in Eq. (6) can be expanded in sequence according to the distribution origin contraction basis set, given as follows:

$$y^k = \sum_{\alpha=1}^{M} c_\alpha \phi_{p,\alpha}, \tag{7}$$

where c_α is contraction coefficient, and α denotes the index of each original function $\phi_{p,\alpha}$. $\phi_{p,\alpha}$ normally takes one of the following two forms:[37]

$$\phi_{p,\alpha} = \mathrm{sech}^{\eta_\alpha}(\gamma_{p,\alpha}\rho_{p,\alpha}), \tag{8}$$

$$\phi_{p,\alpha} = \left[\frac{\tanh(\beta_\alpha R_P)}{R_P}\right]^{\sigma_\alpha} \mathrm{sech}^{\eta_\alpha}(\gamma_{p,\alpha}\rho_{p,\alpha}), \tag{9}$$

where $\gamma_{p,\alpha}$ is the non-linear parameter, $\rho_{p,\alpha} = R_p - R_{p,\alpha}^{\mathrm{ref}}$ denotes the deviation of the coordinate R_p relative the initial coordinate $R_{p,\alpha}^{\mathrm{ref}}$, and the parameters η_α, σ_α and β_α are set to be the values of 1, 6, and 1/5, respectively.[56] Finally, to reduce linear dependence, the origin of the distribution ($R_{p,\alpha}^{\mathrm{ref}}$) is represented by the following expression:

$$R_{p,\alpha}^{\mathrm{ref}} = \zeta (R_p^{\mathrm{ref}})^{\alpha-1}, \tag{10}$$

where the parameters of ζ and R_p^{ref} should be chosen reasonably during the fitting.

III. ANALYSIS OF RESULTS

For high-lying electronic states of N_2 with no available experimental spectroscopic data, the CHIPR method can provide a high-accuracy fitting for *ab initio* data.[36] An example is presented in Fig. 2, which displays the fitting curve for *ab initio* potential energy points of the $G\ ^3\Delta_g$ state [corresponding to $N(^4S)$–$N(^2D)$] by the CHIPR method. It can be observed that the fitted curve is in good agreement with *ab initio* potential energy points, and the root mean square deviation (RMSD) is only 8.26 cm^{-1}.

For low-lying electronic states of N_2, in which experimental spectroscopic data, such as the equilibrium geometry, dissociation energy, vibrational frequency, and vibrational energy levels are available, the CHIPR PECs can be refined using these experimental spectroscopic

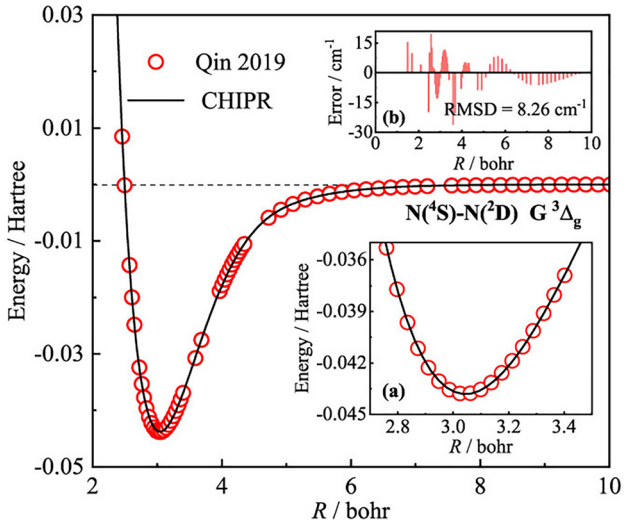

FIG. 2. A combined-hyperbolic-inverse-power-representation potential energy curve (CHIPR PEC) (indicated by a line) for the G $^3\Delta_g$ state [corresponding to N(^{4}S)–N(^{2}D)]. *Ab initio* data were obtained from Qin *et al.*[43] and denoted as circles. The inset (a) exhibits the details of the potential energy well. The inset (b) depicts the deviation between the CHIPR PEC and *ab initio* potential energy points.

data.[36] Figure 3 displays the experimentally refined CHIPR (Er-CHIPR) PEC for the A $^3\Sigma_u^+$ state [corresponding to N(^{4}S)–N(^{4}S)]. In the inset (a), the Er-CHIPR curve deviates slightly from *ab initio* potential energy points after the refinement of *ab initio* data using experimental spectroscopic data. The deviations of the vibrational energy levels obtained from the Er-CHIPR PEC relative to experimental ones are within $\pm 0.2\,\mathrm{cm}^{-1}$, as presented in the inset (b) of Fig. 3.

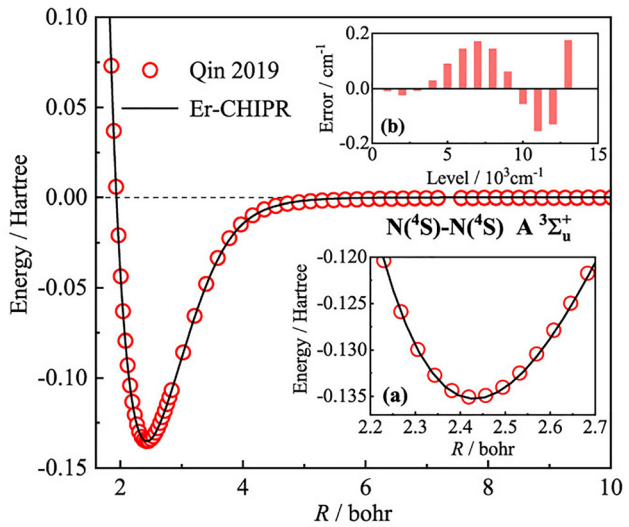

FIG. 3. An experimentally refined combined-hyperbolic-inverse-power-representation potential energy curve (Er-CHIPR PEC) (indicated by a line) for the A $^3\Sigma_u^+$ state [corresponding to N(^{4}S)–N(^{4}S)] based on the experimental spectroscopic data from Lofthus[57] and Miller.[58] *Ab initio* data are from Qin *et al.*[43] and expressed as circles. The inset (a) exhibits the details of the potential well. The inset (b) depicts the deviation between the vibrational energy levels obtained from the Er-CHIPR PEC and experimental ones.

Overall, the CHIPR method can not only give a good fitting of *ab initio* potential energy points along the whole internuclear region but also can refine the obtained CHIPR PEC using available experimental spectroscopic data. Hence, the CHIPR method is a good choice for providing reliable analytical PECs in the calculation of collision integrals. In addition, the widely used potential functions including the HH[27] and MM[32] potentials are also taken into account here. The HH potential energy function is given by

$$V_{HH}(R) = D_e\left[\left(1 - e^{-\alpha(\mathrm{R}/R_e - 1)}\right)^2 + \beta\left(\frac{\mathrm{R}}{R_e} - 1\right)^3 \times \left[1 + \gamma(\mathrm{R}/R_e - 1)\right] e^{-2\alpha(\mathrm{R}/R_e - 1)}\right], \tag{11}$$

where D_e is the potential well depth, r_e is the equilibrium separation, and a, β, and γ are the adjustable parameters obtained either from spectroscopic data or by non-linear fitting. The MM potential energy function is given by

$$V_{MM}(R) = D_e\left[\left(1 \pm e^{-\beta(R-R_e)}\right)^2\right] - D_e, \tag{12}$$

$$\beta = \beta_0\left[1 + \gamma(R - R_e) + \lambda(R - R_e)^2\right], \tag{13}$$

where the "+" sign is for repulsive PECs, and the "−" sign is for bound PECs. β_0 and λ are the adjustable parameters.

Figure 4 displays three different analytical PECs for the X $^1\Sigma_g^+$ state [corresponding to N(^{4}S)–N(^{4}S)], along with *ab initio* potential energy points. Insets (a) and (b) present the details of PECs at short-range (about 1.0–1.6 bohr) and dissociated asymptotic (about 3.0–

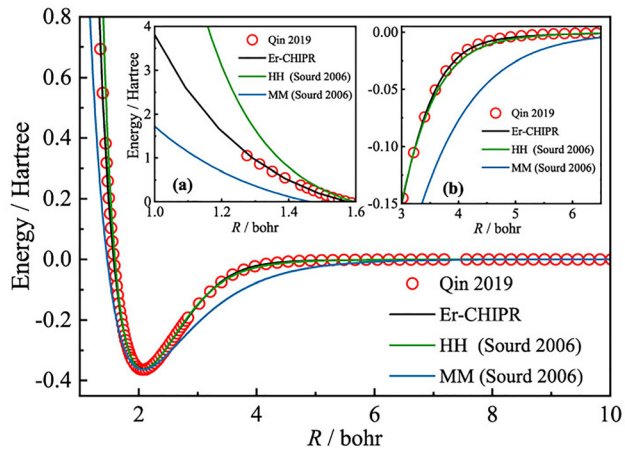

FIG. 4. Potential energy curves for the X $^1\Sigma_g^+$ state [corresponding to N(^{4}S)–N(^{4}S)]: *Ab initio* potential energy points, experimentally refined combined-hyperbolic-inverse-power-representation potential energy curve (Er-CHIPR PEC), Hulburt–Hirschfelder (HH) PEC, and Modified Morse (MM) PEC. *Ab initio* potential energy points are from Qin *et al.*[43] and expressed as circles. All parameters of HH and MM PECs were adopted by Sourd *et al.*[59] Insets (a) and (b) depict the details of the short-range region and dissociated asymptotic region, respectively.

TABLE II. Comparison of collision integrals $\sigma^2\Omega^{(1,1)*}$ (Å^2) for the X $^1\Sigma_g^+$ state corresponding to N(^{4}S)–N(^{4}S) system.

T (K)	Er-CHIPR	HH (Sourd[59])	MM (Sourd[59])
1000	9.735	10.414	15.907
2000	7.361	9.000	13.958
5000	5.550	7.181	11.139
8000	4.968	6.285	9.692
10000	4.722	5.876	8.991
15000	4.272	5.119	7.560
20000	3.906	4.534	6.410
30000	3.263	3.623	4.728
50000	2.344	2.485	2.904

6.5 bohr) regions. The Er-CHIPR PEC was obtained by fitting *ab initio* potential energy points.

Table II provides a comparison of collision integrals $\sigma^2\Omega^{(1,1)*}$ for the X $^1\Sigma_g^+$ state [corresponding to N(^{4}S)–N(^{4}S)] calculated using three different analytical PECs, i.e., the Er-CHIPR PEC, HH PEC, and MM PEC. There exist significant differences for the collision integrals obtained using these three analytical PECs at low temperatures. In particular, the collision integrals obtained from MM PEC are more than twice that obtained from the Er-CHIPR PEC at low temperatures, which indicates that the collision integrals at low temperatures are more sensitive to the shape of the PECs. With the increase in temperature, such difference gradually decreases, but still exists. Recently, Buchowiecki *et al.*[33] pointed out the importance of accurately describing the PECs in short-range regions in calculating the collision integrals. Hence, reliable analytical modeling of the PECs is desired.

In our subsequent calculation of collision integrals, the CHIPR method was chosen to fit *ab initio* potential energy points. A total of 24 electronic states correlating to the N(^{4}S)–N(^{4}S), N(^{4}S)–N(^{2}D), and N(^{4}S)–N(^{2}P) dissociation limits were considered and their *ab initio* potential energy points were obtained by the high-level MRCI calculations and fitted using the CHIPR method. The CHIPR PECs of the X $^1\Sigma_g^+$, A $^3\Sigma_u^+$, B $^3\Pi_g$, W $^3\Delta_u$, C″ $^5\Pi_u$, and B′ $^3\Sigma_u^-$ states were also refined using available experimental spectroscopic data. The obtained

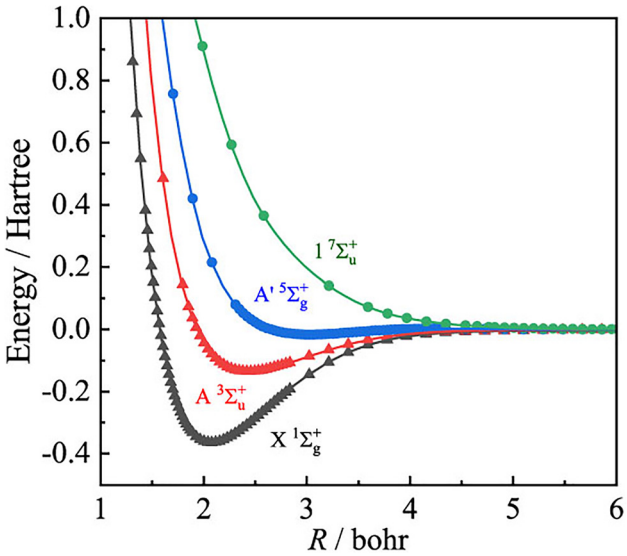

FIG. 5. The (or experimentally refined) combined-hyperbolic-inverse-power-representation potential energy curves (CHIPR or Er-CHIPR PECs) for the electronic states corresponding to N(^{4}S)–N(^{4}S). The solid lines represent CHIPR or Er-CHIPR PECs, where the curves of X $^1\Sigma_g^+$ and A $^3\Sigma_u^+$ were refined using available experimental spectroscopic data.[57,58] The triangles and circles represent *ab initio* data, where data of triple states are from Qin *et al.*[43] and data represented by circles are computed in this work.

ab initio potential energy points and CHIPR PECs are displayed in Figs. 5–7, in which PECs are not completely given for clarity. The details of *ab initio* potential energy points, CHIPR PECs and the relevant fitting parameters are given in the supplementary material.

It can be noticed that the CHIPR (or Er-CHIPR) PECs are all in good agreement with *ab initio* potential energy points. In particular, the CHIPR method can also provide a good fit for non-Morse potentials, such as A′ $^5\Sigma_u^+$, C $^3\Pi_u$, E $^3\Sigma_g^+$, and 1 $^5\Delta_u$, etc. (see Figs. S1–S3 in the supplementary material), while the commonly used analytical potential energy functions, such as LJ, m-6–8 HH, MS, and MM functions, cannot guarantee suitable fits for these PECs. The RMSDs of the

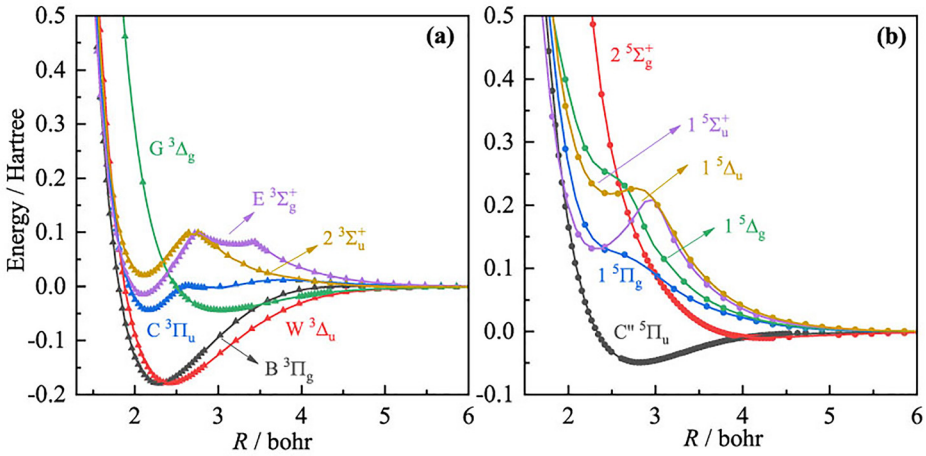

FIG. 6. The (experimentally refined) combined-hyperbolic-inverse-power-representation potential energy curves (CHIPR or Er-CHIPR PECs) for (a) triplet states and (b) quintet states corresponding to N(^{4}S)–N(^{2}D). The solid lines represent CHIPR or Er-CHIPR PECs, where the curves of B $^3\Pi_g$, W $^3\Delta_u$ and C″ $^5\Pi_u$ were refined using available experimental spectroscopic data.[57,60,61] The triangles and circles represent *ab initio* data, where data of triple states are from Qin *et al.*[43] and data represented by circles are computed in this work.

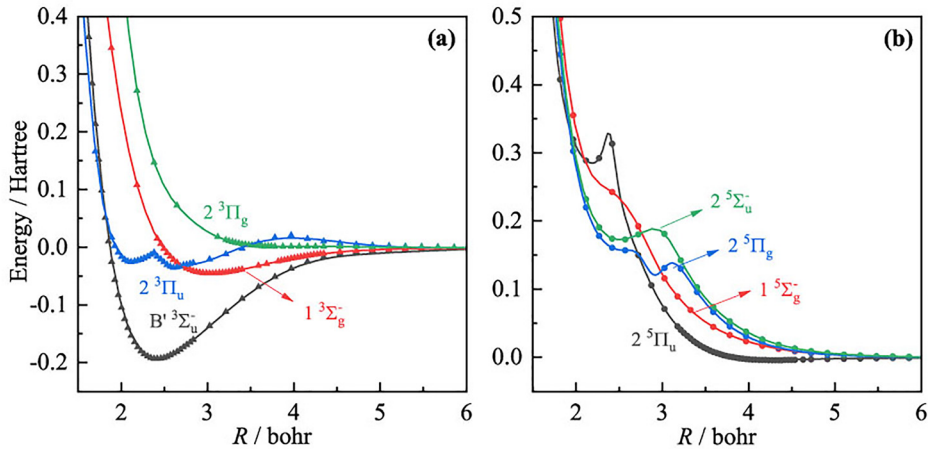

FIG. 7. The (experimentally refined) combined-hyperbolic-inverse-power-representation potential energy curves (CHIPR or Er-CHIPR PECs) for (a) triplet states and (b) quintet states corresponding to N(^{4}S)–N(^{2}P). The solid lines represent CHIPR or Er-CHIPR PECs, where the curves of B′ $^3\Sigma_u^-$ was refined using available experimental spectroscopic data.[57] The triangles and circles represent *ab initio* data, where data of triple states are from Qin *et al.*[43] and data represented by circles are computed in this work.

CHIPR PECs with *ab initio* data are less than 20 cm^{-1} except for the non-Morse potentials such as A′ $^5\Sigma_u^+$, C $^3\Pi_u$, E $^3\Sigma_g^+$, and 1 $^5\Delta_u$, etc.

Table III compares several collision integrals with those in the literature.[15,22,62] The collisional integrals from Levin *et al.*[15] were obtained using a spline fitting of potential energy data, in which experimental ones for X $^1\Sigma_g^+$ and A $^3\Sigma_u^+$ and *ab initio* ones for A′ $^5\Sigma_g^+$ and 1 $^7\Sigma_u^+$ were used.[57,63–65] Capitelli *et al.*[62] obtained the collisional integrals using the Morse potential function, LJ potential function and exponential repulsive function, in which the LJ potential function was used to compute collision integrals at temperatures below 1000 K. These functions were all obtained based on the experimental spectroscopic data for the bound states[66] and theoretical potential energies for the repulsive septet state.[67] Buchowiecki *et al.*[22] reported the collision integrals using the HH potential energy function, which were constructed based on the spectroscopic data from Sourd.[59] As shown in Table III, the difference between our collision integrals and those from Levin *et al.*[15] is within 5% at any temperature. The maximum difference between our collisional integral and that from Capitelli *et al.*[62] occurs at 6000 K and is about 13%. Table IV presents the collision integrals relevant to the first excited dissociation limit for N(^{4}S)–N(^{2}D). The collision integrals from Laricchiuta *et al.*[23] and Sourd *et al.*[24] were obtained with the traditional multipotential approach. The overall deviation is not significant, where the largest difference is 23% at 20 000 K with the results of Sourd *et al.*[24] The main source of deviation between the present work and their calculations is from the differences of the PECs in the short-range regions, which were obtained by the different analytical potential energy functions. These deviations make the collision integral subject to short-range and long-range interactions with large uncertainties in the high and low-temperature regions, respectively. The collision integrals of N(^{4}S)–N(^{2}D) and N(^{4}S)–N(^{2}P) interactions were also calculated using the CHIPR PECs for temperatures at 500–50 000 K. Figure 8 illustrates the collision integrals of N(^{4}S)–N(^{4}S), N(^{4}S)–N(^{2}D), and N(^{4}S)–N(^{2}P) systems vs the temperature. All collision integrals decrease with the increasing temperature in the temperature range of 500–50 000 K. The obtained collision integrals for the N(^{4}S)–N(^{4}S), N(^{4}S)–N(^{2}D), and N(^{4}S)–N(^{2}P) interactions are also tabulated in the Appendix. By using the CHIPR method to fit high-level *ab initio* potential energy points of N_2 and simultaneously refining the PECs using available experimental spectroscopic data, we can provide reliable collision integrals in the temperature interval below 50 000 K.

TABLE III. Collision integrals $\sigma^2\Omega^{(1,1)*}$ (Å^2) for the interaction of N(^{4}S)–N(^{4}S).

T (K)	This work	Levin[15]	Buchowiecki[22]	Capitelli[62]
500	7.191	7.033	7.67	7.76
1000	6.112	5.962	6.65	6.79
2000	5.157	5.145	5.69	5.25
4000	4.340	4.388	4.73	4.50
5000	4.096	4.140	4.44	4.27
6000	3.900	3.936	4.21	3.45
8000	3.596	3.614	3.85	3.26
10000	3.362	3.366	3.59	3.55
20000	2.639	2.619	2.80	2.81
50000	1.801	1.769	···	2.00

IV. CONCLUSIONS

In this work, we have constructed the PECs of 24 electronic states correlating to N(^{4}S)–N(^{4}S), N(^{4}S)–N(^{2}D), and N(^{4}S)–N(^{2}P) by the CHIPR method, in which PECs of some low-lying electronic states were also refined using available experimental spectroscopic data. The analysis of collision integrals using different analytical potential energy

TABLE IV. Collision integrals $\sigma^2\Omega^{(2,2)*}$ (Å^2) for the interaction of N(^{4}S)–N(^{2}D).

T (K)	Er-CHIPR	Laricchiuta[23]	Sourd[24]
1000	8.043	7.0348	6.8684
2000	6.682	5.8568	5.6967
4000	5.472	4.6625	4.6980
6000	4.826	4.0365	4.1260
9000	4.211	3.4940	3.5547
10000	4.057	3.3650	3.4099
20000	3.062	2.5874	2.4890

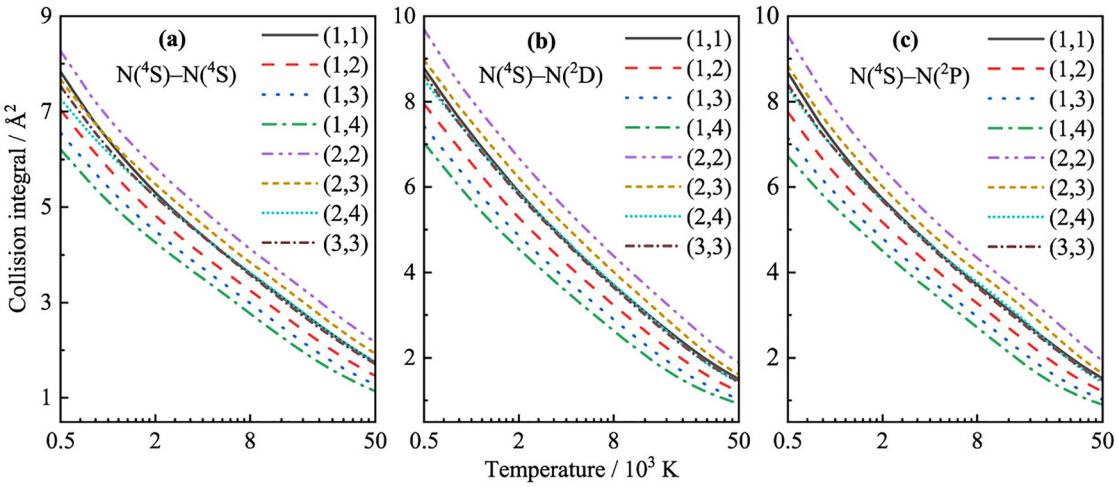

FIG. 8. The collision integrals of (a) N(^{4}S)–N(^{4}S), (b) N(^{4}S)–N(^{2}D), and (c) N(^{4}S)–N(^{2}P) obtained using (experimentally refined) combined-hyperbolic-inverse-power-representation potential energy curves (CHIPR or Er-CHIPR PECs).

TABLE V. N(^{4}S)–N(^{4}S) transport collision integrals (Å^2).

T (K)	$\sigma^2\Omega^{(1,1)*}$	$\sigma^2\Omega^{(1,2)*}$	$\sigma^2\Omega^{(1,3)*}$	$\sigma^2\Omega^{(1,4)*}$	$\sigma^2\Omega^{(2,2)*}$	$\sigma^2\Omega^{(2,3)*}$	$\sigma^2\Omega^{(2,4)*}$	$\sigma^2\Omega^{(3,3)*}$
500	7.824	7.037	6.560	6.206	8.265	7.668	7.265	7.531
800	6.831	6.190	5.766	5.445	7.277	6.809	6.478	6.622
900	6.611	5.995	5.580	5.270	7.061	6.617	6.300	6.412
1000	6.417	5.821	5.419	5.120	6.879	6.453	6.146	6.235
1100	6.251	5.671	5.279	4.989	6.720	6.308	6.009	6.080
1200	6.100	5.537	5.155	4.874	6.578	6.180	5.888	5.940
1300	5.967	5.415	5.044	4.771	6.448	6.062	5.778	5.818
1400	5.845	5.305	4.943	4.677	6.338	5.961	5.680	5.707
1500	5.736	5.209	4.853	4.593	6.234	5.862	5.588	5.608
1600	5.632	5.117	4.770	4.516	6.137	5.775	5.507	5.517
1700	5.541	5.034	4.695	4.444	6.054	5.693	5.428	5.432
1800	5.454	4.956	4.623	4.377	5.972	5.619	5.357	5.355
1900	5.375	4.885	4.557	4.317	5.896	5.549	5.289	5.282
2000	5.297	4.818	4.496	4.257	5.828	5.481	5.223	5.216
2500	4.989	4.541	4.236	4.008	5.527	5.202	4.955	4.937
3000	4.750	4.323	4.032	3.812	5.293	4.977	4.734	4.717
3500	4.554	4.145	3.863	3.647	5.101	4.791	4.550	4.536
4000	4.395	3.998	3.721	3.508	4.938	4.631	4.392	4.382
4500	4.256	3.867	3.595	3.384	4.794	4.490	4.255	4.244
5000	4.138	3.753	3.485	3.274	4.668	4.367	4.135	4.122
5500	4.026	3.651	3.384	3.173	4.547	4.257	4.029	4.012
6000	3.929	3.558	3.292	3.080	4.452	4.158	3.934	3.911
7000	3.759	3.394	3.128	2.915	4.273	3.988	3.770	3.734
7500	3.685	3.321	3.054	2.840	4.195	3.914	3.698	3.654
8000	3.614	3.252	2.985	2.770	4.123	3.845	3.631	3.581
8500	3.548	3.187	2.921	2.704	4.055	3.780	3.566	3.511
9000	3.486	3.126	2.858	2.642	3.991	3.718	3.506	3.446
9500	3.428	3.068	2.799	2.583	3.933	3.661	3.448	3.385
10000	3.372	3.013	2.744	2.528	3.877	3.607	3.394	3.326
15000	2.936	2.578	2.313	2.106	3.440	3.169	2.952	2.877

TABLE V. (*Continued.*)

T (K)	$\sigma^2\Omega^{(1,1)*}$	$\sigma^2\Omega^{(1,2)*}$	$\sigma^2\Omega^{(1,3)*}$	$\sigma^2\Omega^{(1,4)*}$	$\sigma^2\Omega^{(2,2)*}$	$\sigma^2\Omega^{(2,3)*}$	$\sigma^2\Omega^{(2,4)*}$	$\sigma^2\Omega^{(3,3)*}$
20000	2.629	2.278	2.024	1.830	3.128	2.856	2.639	2.570
25000	2.396	2.057	1.816	1.636	2.885	2.615	2.401	2.341
30000	2.214	1.885	1.657	1.490	2.689	2.423	2.215	2.163
35000	2.065	1.749	1.533	1.376	2.527	2.265	2.064	2.019
40000	1.941	1.636	1.431	1.283	2.389	2.133	1.940	1.899
45000	1.835	1.542	1.346	1.206	2.270	2.022	1.835	1.797
50000	1.744	1.461	1.274	1.140	2.167	1.925	1.746	1.710

TABLE VI. N(^{4}S)–N(^{2}D) transport collision integrals (Å^2).

T (K)	$\sigma^2\Omega^{(1,1)*}$	$\sigma^2\Omega^{(1,2)*}$	$\sigma^2\Omega^{(1,3)*}$	$\sigma^2\Omega^{(1,4)*}$	$\sigma^2\Omega^{(2,2)*}$	$\sigma^2\Omega^{(2,3)*}$	$\sigma^2\Omega^{(2,4)*}$	$\sigma^2\Omega^{(3,3)*}$
500	8.770	7.943	7.422	7.032	9.678	8.967	8.498	8.636
800	7.704	6.995	6.496	6.100	8.516	7.967	7.568	7.579
900	7.455	6.760	6.265	5.874	8.264	7.734	7.340	7.332
1000	7.238	6.552	6.061	5.677	8.043	7.527	7.137	7.114
1100	7.042	6.366	5.880	5.506	7.848	7.341	6.953	6.922
1200	6.864	6.197	5.718	5.354	7.672	7.174	6.786	6.751
1300	6.707	6.046	5.574	5.218	7.513	7.018	6.633	6.597
1400	6.562	5.907	5.444	5.098	7.366	6.875	6.493	6.456
1500	6.426	5.781	5.326	4.986	7.230	6.744	6.365	6.328
1600	6.301	5.664	5.218	4.886	7.108	6.624	6.249	6.210
1700	6.186	5.557	5.119	4.793	6.991	6.510	6.138	6.099
1800	6.080	5.458	5.026	4.707	6.881	6.405	6.037	5.997
1900	5.977	5.365	4.940	4.627	6.778	6.305	5.942	5.903
2000	5.885	5.279	4.861	4.551	6.682	6.213	5.855	5.814
2500	5.491	4.917	4.522	4.224	6.272	5.824	5.485	5.433
3000	5.183	4.634	4.254	3.962	5.952	5.521	5.194	5.134
3500	4.934	4.402	4.030	3.742	5.690	5.272	4.955	4.888
4000	4.723	4.205	3.840	3.557	5.472	5.062	4.748	4.677
4500	4.542	4.035	3.675	3.395	5.279	4.878	4.568	4.497
5000	4.384	3.884	3.529	3.254	5.111	4.715	4.408	4.338
5500	4.243	3.749	3.399	3.127	4.961	4.570	4.267	4.196
6000	4.114	3.628	3.281	3.012	4.826	4.439	4.138	4.068
7000	3.891	3.416	3.075	2.809	4.588	4.209	3.914	3.843
7500	3.793	3.322	2.983	2.719	4.485	4.107	3.814	3.743
8000	3.702	3.235	2.897	2.633	4.387	4.012	3.721	3.649
8500	3.618	3.154	2.818	2.555	4.297	3.924	3.636	3.563
9000	3.538	3.077	2.743	2.481	4.211	3.842	3.555	3.482
9500	3.464	3.005	2.672	2.412	4.132	3.763	3.477	3.405
10000	3.393	2.937	2.606	2.346	4.057	3.690	3.404	3.332
15000	2.849	2.412	2.098	1.860	3.472	3.114	2.830	2.777
20000	2.480	2.063	1.773	1.562	3.062	2.707	2.427	2.406
25000	2.208	1.815	1.551	1.364	2.750	2.401	2.133	2.136
30000	2.000	1.631	1.390	1.224	2.499	2.164	1.913	1.930
35000	1.835	1.489	1.269	1.120	2.296	1.976	1.743	1.768
40000	1.700	1.376	1.175	1.040	2.130	1.826	1.610	1.637
45000	1.589	1.285	1.099	0.976	1.991	1.704	1.504	1.530
50000	1.496	1.209	1.037	0.924	1.873	1.602	1.417	1.440

TABLE VII. N(^{4}S)–N(^{2}P) transport collision integrals (Å^2).

T (K)	$\sigma^2\Omega^{(1,1)*}$	$\sigma^2\Omega^{(1,2)*}$	$\sigma^2\Omega^{(1,3)*}$	$\sigma^2\Omega^{(1,4)*}$	$\sigma^2\Omega^{(2,2)*}$	$\sigma^2\Omega^{(2,3)*}$	$\sigma^2\Omega^{(2,4)*}$	$\sigma^2\Omega^{(3,3)*}$
500	8.678	7.758	7.153	6.718	9.549	8.828	8.313	8.397
800	7.491	6.726	6.232	5.875	8.317	7.721	7.294	7.314
900	7.227	6.498	6.025	5.684	8.044	7.477	7.064	7.076
1000	7.001	6.303	5.849	5.521	7.809	7.263	6.867	6.874
1100	6.805	6.132	5.694	5.375	7.604	7.077	6.691	6.696
1200	6.633	5.983	5.557	5.243	7.424	6.912	6.536	6.539
1300	6.479	5.848	5.433	5.124	7.262	6.763	6.397	6.397
1400	6.339	5.725	5.319	5.018	7.115	6.628	6.265	6.268
1500	6.215	5.616	5.216	4.915	6.982	6.505	6.144	6.150
1600	6.101	5.513	5.120	4.823	6.859	6.390	6.039	6.039
1700	5.994	5.419	5.030	4.735	6.748	6.283	5.939	5.939
1800	5.896	5.329	4.946	4.654	6.642	6.185	5.844	5.845
1900	5.805	5.247	4.867	4.578	6.544	6.094	5.756	5.757
2000	5.719	5.170	4.792	4.505	6.451	6.008	5.674	5.673
2500	5.361	4.839	4.475	4.195	6.066	5.644	5.326	5.317
3000	5.080	4.577	4.221	3.946	5.767	5.362	5.054	5.033
3500	4.852	4.361	4.013	3.744	5.519	5.128	4.832	4.801
4000	4.656	4.176	3.835	3.573	5.314	4.933	4.646	4.605
4500	4.488	4.016	3.682	3.425	5.138	4.766	4.485	4.436
5000	4.341	3.877	3.548	3.294	4.983	4.620	4.346	4.288
5500	4.209	3.753	3.428	3.177	4.846	4.492	4.226	4.156
6000	4.091	3.640	3.318	3.069	4.724	4.377	4.117	4.038
7000	3.885	3.443	3.127	2.878	4.514	4.181	3.930	3.831
7500	3.794	3.356	3.040	2.790	4.423	4.095	3.848	3.740
8000	3.709	3.275	2.959	2.709	4.340	4.017	3.773	3.653
8500	3.631	3.198	2.884	2.631	4.261	3.942	3.700	3.576
9000	3.557	3.126	2.811	2.558	4.189	3.872	3.629	3.499
9500	3.487	3.059	2.742	2.488	4.121	3.808	3.565	3.429
10000	3.421	2.993	2.677	2.423	4.058	3.747	3.501	3.362
15000	2.904	2.480	2.164	1.916	3.548	3.228	2.958	2.842
20000	2.539	2.122	1.819	1.592	3.169	2.829	2.544	2.480
25000	2.264	1.861	1.579	1.376	2.861	2.510	2.225	2.206
30000	2.048	1.663	1.404	1.223	2.605	2.256	1.982	1.991
35000	1.874	1.510	1.272	1.111	2.391	2.050	1.793	1.819
40000	1.732	1.388	1.170	1.025	2.213	1.884	1.644	1.679
45000	1.615	1.290	1.089	0.957	2.061	1.747	1.524	1.563
50000	1.515	1.208	1.022	0.902	1.932	1.634	1.426	1.466

functions shows collision integrals are sensitive to the trend of PECs. For PECs in dissociated asymptotic and short-range regions, experimental spectroscopic data are difficult to obtain. Hence, *ab initio* potential energy data can be accepted as a benchmark to guide analytical potential energy functions. This work used the CHIPR method to fit high-level *ab initio* potential energy points of N_2 and simultaneously refining the PECs using available experimental spectroscopic data. Collision integrals are then calculated for N(^{4}S)–N(^{4}S), N(^{4}S)–N(^{2}D), and N(^{4}S)–N(^{2}P) at 500–50 000 K, in which the interactions between the excited atoms N(^{2}P) and ground N(^{4}S) are considered for the first time. Overall, our collision integrals are reliable and can provide a basis for computing transport properties for N-containing high-temperature plasmas.

SUPPLEMENTARY MATERIAL

See the supplementary material for detailed CHIPR (Er-CHIPR) curves of N(^{4}S)–N(^{4}S), N(^{4}S)–N(^{2}D), and N(^{4}S)–N(^{2}P) interactions.

ACKNOWLEDGMENTS

We acknowledge Marcin Buchowiecki and Péter Szabó for providing the code and useful suggestions. This work was

sponsored by the National Natural Science Foundation of China (No. 52106098), Natural Science Foundation of Shandong Province (No. ZR2021QE021), and Postdoctoral Innovation Project of Shandong Province and Postdoctoral Applied Research Project of Qingdao City. The scientific calculations in this paper have been done on the HPC Cloud Platform of Shandong University.

AUTHOR DECLARATIONS

Conflict of Interest

The authors have no conflicts to disclose.

Author Contributions

Zi Ding: Formal analysis (equal); Investigation (equal); Methodology (equal); Software (equal); Writing – original draft (equal). **Zhi Qin:** Conceptualization (equal); Methodology (equal); Supervision (equal); Writing – review & editing (equal). **Linhua Liu:** Funding acquisition (equal); Supervision (equal); Writing – review & editing (equal).

DATA AVAILABILITY

The data that support the findings of this study are available within the article and its supplementary material.

APPENDIX: TRANSPORT COLLISION INTEGRALS AT 500–50 000 K

Tables V–VII provide the transport collision integrals (Å^2) for N(^{4}S)–N(^{4}S), N(^{4}S)–N (^{2}D), and N(^{4}S)–N(^{2}P) at 500–50 000 K, respectively.

REFERENCES

[1] S. Sun, J. Zhang, and M. Ni, "Solidification of liquid metal droplet during impact in the presence of vertical magnetic field," Phys. Fluids **34**, 052106 (2022).
[2] W. Shen, L. Yu, H. Liu, Y. He, Z. Zhou, and Q. Zhang, "Diffusion welding of powder metallurgy high speed steel by spark plasma sintering," J. Mater. Process. Technol. **275**, 116383 (2020).
[3] D. T. Young, J. E. Nordholt, J. L. Burch, D. J. McComas, R. P. Bowman, R. A. Abeyta, J. Alexander, J. Baldonado, P. Barker, and R. K. Black, "Plasma experiment for planetary exploration (PEPE)," Space Sci. Rev. **129**, 327 (2007).
[4] L. Xie, H. Liang, H. Zong, X. Liu, and Y. Li, "Multipurpose distributed dielectric-barrier-discharge plasma actuation: Icing sensing, anti-icing, and flow control in one," Phys. Fluids **34**, 071701 (2022).
[5] B. Xu, S. Chen, S. Tashiro, F. Jiang, and M. Tanaka, "Physical mechanism of material flow in variable polarity plasma arc keyhole welding revealed by *in situ* x-ray imaging," Phys. Fluids **33**, 17121 (2021).
[6] Y. Wang, Y. Li, J. Liu, and Y. Li, "On the receptivity of surface plasma actuation in high-speed boundary layers," Phys. Fluids **32**, 094102 (2020).
[7] L. Dong, K. Choi, and Y. Wang, "Plasma flow control of the tip vortices over a very low aspect-ratio wing," Phys. Fluids **34**, 087101 (2022).
[8] G. Bird, "Computation of electron density in high altitude re-entry flows," AIAA Paper No. 89-1882, 1989.
[9] W. J. McDoniel, D. B. Goldstein, P. L. Varghese, and L. M. Trafton, "Simulation of Io's plumes and Jupiter's plasma torus," Phys. Fluids **31**, 077103 (2019).
[10] B. Wei, Y. Wu, H. Liang, J. Chen, G. Zhao, M. Tian, and H. Xu, "Performance and mechanism analysis of nanosecond pulsed surface dielectric barrier discharge based plasma deicer," Phys. Fluids **31**, 091701 (2019).
[11] Y. Wang, H. Zhang, Y. Wu, Y. Li, and Y. Zhu, "Supersonic compressor cascade flow control using plasma actuation at low Reynolds number," Phys. Fluids **34**, 027105 (2022).
[12] J. Tian, W. Liu, W. Zhang, and X. Jiang, "Study of formation mechanism of double metal plasma jets in a low-current pulsed vacuum arc discharge," Phys. Fluids **33**, 037103 (2021).
[13] G. Bellas Chatzigeorgis, J. B. Haskins, and J. B. Scoggins, "Transport properties for neutral C, H, N, O, and Si-containing species and mixtures from the Gordon and McBride thermodynamic database," Phys. Fluids **34**, 087106 (2022).
[14] A. Bellemans, J. B. Scoggins, R. L. Jaffe, and T. E. Magin, "Transport properties of carbon-phenolic gas mixtures," Phys. Fluids **31**, 096102 (2019).
[15] E. Levin, H. Partridge, and J. R. Stallcop, "Collision integrals and high temperature transport properties for NN, OO, and NO," J. Thermophys. Heat Transfer **4**, 469 (1990).
[16] M. Capitelli, D. Bruno, and A. Laricchiuta, "Transport cross sections: Classical and quantum approaches," in *Fundamental Aspects of Plasma Chemical Physics* (Springer, 2013), pp. 57–98.
[17] J. Kim, O. Kwon, and C. Park, "A high temperature elastic collision model for DSMC based on collision integrals," AIAA Paper No. 2006-3803, 2006.
[18] M. Pfeiffer, "An optimized collision-averaged variable soft sphere parameter set for air, carbon and corresponding ionized species," Phys. Fluids **34**, 117110 (2022).
[19] J. O. Hirschfelder, "Heat conductivity in polyatomic or electronically excited gases. II," J. Chem. Phys. **26**, 282 (1957).
[20] V. A. Istomin, E. V. Kustova, and M. A. Mekhonoshina, "Eucken correction in high-temperature gases with electronic excitation," J. Chem. Phys. **140**, 184311 (2014).
[21] V. A. Istomin and E. V. Kustova, "State-specific transport properties of partially ionized flows of electronically excited atomic gases," Chem. Phys. **485**, 125–139 (2017).
[22] M. Buchowiecki, "High-temperature collision integrals for m-6-8 and Hulburt–Hirschfelder potentials," Int. J. Thermophys. **43**, 38 (2022).
[23] A. Laricchiuta, F. Pirani, G. Colonna, D. Bruno, C. Gorse, R. Celiberto, and M. Capitelli, "Collision integrals for interactions involving atoms in electronically excited states," J. Phys. Chem. A **113**, 15250 (2009).
[24] B. Sourd, P. André, J. Aubreton, and M. Elchinger, "Influence of the excited states of atomic nitrogen N (^{2}D) and N (^{2}P) on the transport properties of nitrogen. Part I: Atomic nitrogen properties," Plasma Chem. Plasma Process. **27**, 35 (2007).
[25] L. S. Tee, S. Gotoh, and W. E. Stewart, "Molecular parameters for normal fluids. Lennard-Jones 12-6 potential," Ind. Eng. Chem. Fundam. **5**, 356 (1966).
[26] V. A. Petrov, O. A. Ranjbar, P. A. Zhilyaev, and A. N. Volkov, "Kinetic simulations of laser-induced plume expansion from a copper target into a vacuum or argon background gas based on *ab initio* calculation of Cu–Cu, Ar–Ar, and Ar–Cu interactions," Phys. Fluids **32**, 102010 (2020).
[27] H. M. Hulburt and J. O. Hirschfelder, "Potential energy functions for diatomic molecules," J. Chem. Phys. **9**, 61 (1941).
[28] J. C. Rainwater, P. M. Holland, and L. Biolsi, "Binary collision dynamics and numerical evaluation of dilute gas transport properties for potentials with multiple extrema," J. Chem. Phys. **77**, 434 (1982).
[29] U. Hohm, "Mutual intersection points of reduced collision integrals for Lennard–Jones (nm), Hulburt–Hirschfelder, and Tang–Toennies potential energy functions," Int. J. Thermophys. **43**, 147 (2022).
[30] J. G. Kim and G. Park, "Thermochemical nonequilibrium parameter modification of oxygen for a two-temperature model," Phys. Fluids **30**, 016101 (2018).
[31] T. Lim, "Application of extended-Rydberg parameters in general Morse potential functions," J. Math. Chem. **49**, 1086 (2011).
[32] P. J. Kuntz and A. C. Roach, "Ion-molecule reactions of the rare gases with hydrogen. Part 1—Diatomics-in-molecules potential energy surface for ArH^+_2," J. Chem. Soc., Faraday Trans. 2 **68**, 259 (1972).
[33] B. Marcin and P. Szabó, "N–H collision integrals with study of repulsive interactions," Plasma Sources Sci. Technol. **31**, 45010 (2022).
[34] M. J. Wright, H. H. Hwang, and D. W. Schwenke, "Recommended collision integrals for transport property computations. Part II: Mars and Venus entries," AIAA J. **45**, 281 (2007).
[35] R. A. Aziz, A. R. Janzen, and M. R. Moldover, "*Ab initio* calculations for helium: A standard for transport property measurements," Phys. Rev. Lett. **74**, 1586 (1995).

[36]C. M. Rocha and A. J. C. Varandas, "A general code for fitting global potential energy surfaces via CHIPR method: Direct-fit diatomic and tetratomic molecules," Comput. Phys. Commun. **258**, 107556 (2021).

[37]C. M. Rocha and A. J. C. Varandas, "A general code for fitting global potential energy surfaces via CHIPR method: Triatomic molecules," Comput. Phys. Commun. **247**, 106913 (2020).

[38]A. J. C. Varandas, "Combined-hyperbolic-inverse-power-representation of potential energy surfaces: A preliminary assessment for H_3 and HO_2," J. Chem. Phys. **138**, 054120 (2013).

[39]G. Chen, Z. Qin, J. Li, and L. Liu, "A global CHIPR potential energy surface of PH_2 ($X\ ^2B_1$) via extrapolation to the complete basis set limit and the dynamics of $P(^2D) + H_2(X^1\Sigma_g^+) \rightarrow PH(X^3\Sigma^-) + H(^2S)$," Phys. Chem. Chem. Phys. **24**, 19371 (2022).

[40]H. Friedrich and H. Friedrich, *Theoretical Atomic Physics* (Springer, Berlin, 2006).

[41]J. O. Hirschfelder, C. F. Curtiss, and R. B. Bird, "Molecular theory of gases and liquids," in *Molecular Theory of Gases and Liquids* (Wiley, 1964).

[42]G. Herzberg, *Molecular Spectra and Molecular Structure. I Spectra of Diatomic Molecules* (Van Nosttarand, New York, 1950).

[43]Z. Qin, J. Zhao, and L. Liu, "Radiative transition probabilities between low-lying electronic states of N_2," Mol. Phys. **117**, 2418 (2019).

[44]H. J. Werner, P. J. Knowles, G. Knizia, F. R. Manby, M. Schütz, P. Celani, W. Györffy, D. Kats, T. Korona, and R. Lindh, *MOLPRO, Version 2015.1, a Package of Ab Initio Programs* [University of Cardiff Chemistry Consultants (UC3), Cardiff, Wales, UK, 2015].

[45]H. J. Werner, P. J. Knowles, G. Knizia, F. R. Manby, and M. Schütz, "Molpro: A general-purpose quantum chemistry program package," Wiley Interdiscip. Rev.: Comput. Mol. Sci. **2**, 242 (2012).

[46]D. E. Woon and T. H. Dunning, Jr., "Gaussian basis sets for use in correlated molecular calculations. III. The atoms aluminum through argon," J. Chem. Phys. **98**, 1358 (1993).

[47]T. Van Mourik, A. K. Wilson, and T. H. Dunning, JR, "Benchmark calculations with correlated molecular wavefunctions. XIII. Potential energy curves for He_2, Ne_2 and Ar_2 using correlation consistent basis sets through augmented sextuple zeta," Mol. Phys **96**, 529 (1999).

[48]D. E. Woon and T. H. Dunning, Jr., "Gaussian basis sets for use in correlated molecular calculations. V. Core-valence basis sets for boron through neon," J. Chem. Phys. **103**, 4572 (1995).

[49]M. Douglas and N. M. Kroll, "Quantum electrodynamical corrections to the fine structure of helium," Ann. Phys. **82**, 89 (1974).

[50]M. Reiher and A. Wolf, "Exact decoupling of the Dirac Hamiltonian. II. The generalized Douglas–Kroll–Hess transformation up to arbitrary order," J. Chem. Phys. **121**, 10945 (2004).

[51]M. Reiher and A. Wolf, "Exact decoupling of the Dirac Hamiltonian," J. Chem. Phys. **121**, 2037 (2004).

[52]M. Hochlaf, H. Ndome, D. Hammoutène, and M. Vervloet, "Valence–Rydberg electronic states of N_2: Spectroscopy and spin–orbit couplings," J. Phys. B **43**, 245101 (2010).

[53]R. S. da Silva, L. R. Ventura, C. E. Fellows, and M. Y. Ballester, "A novel investigation of the N_2 ($C^3\Pi_u - B^3\Pi_g$) and N_2 ($C''^5\Pi_u - A'\ ^5\Sigma_g^+$) band systems using accurate functional forms," J. Quant. Spectrosc. Radiative Transfer **253**, 107130 (2020).

[54]J. N. Murrell, *Molecular Potential Energy Functions* (Wiley, Chichester, 1984).

[55]M. Agúndez, J. Cernicharo, L. Decin, P. Encrenaz, and D. Teyssier, "Confirmation of circumstellar phosphine," Astrophys. J. Lett. **790**, L27 (2014).

[56]A. J. C. Varandas, "Putting together the pieces: A global description of valence and long-range forces via combined hyperbolic inverse power representation of the potential energy surface," in *Reaction Rate Constant Computations: Theories and Applications*, edited by K. Han and T. Chu (The Royal Society of Chemistry, 2013), Chap. 17, pp. 408–445.

[57]A. Lofthus and P. H. Krupenie, "The spectrum of molecular nitrogen," J. Phys. Chem. Ref. Data **6**, 113 (1977).

[58]R. E. Miller, "High-resolution emission Vegard–Kaplan bands of nitrogen," J. Chem. Phys. **43**, 1695 (1965).

[59]B. Sourd, J. Aubreton, M. Elchinger, M. Labrot, and U. Michon, "High temperature transport coefficients in e/C/H/N/O mixtures," J. Phys. D **39**, 1105 (2006).

[60]F. Roux and F. Michaud, " Extension of the analysis of the $B'\ ^3\Sigma_u^- \rightarrow B\ ^3\Pi_g$ and $W\ ^3\Delta_u \rightleftharpoons B\ ^3\Pi_g$ systems of the nitrogen molecule by Fourier transform spectrometry," J. Mol. Spectrosc. **129**, 119 (1988).

[61]K. P. Huber and M. Vervloet, "High-resolution Fourier transform spectroscopy of supersonic jets. The $C''\ ^5\Pi_{ui} \rightarrow A'\ ^5\Sigma_g^+$ Herman infrared bands of $^{14}N_2$," J. Mol. Spectrosc. **153**, 17–25 (1992).

[62]M. Capitelli, C. Gorse, S. Longo, and D. Giordano, "Collision integrals of high-temperature air species," J. Thermophys. Heat Transfer **14**, 259 (2000).

[63]K. Huber and G. Herzberg, *Molecular Spectra and Molecular Structure: IV. Constants of Diatomic Molecules* (Springer, New York, 1979).

[64]F. Roux, F. Michaud, and J. Verges, "High-resolution Fourier spectrometry of $^{14}N_2$ infrared emission spectrum: Extensive analysis of the $B\ ^3\Pi_g$-$A\ ^3\Sigma_u^+$ system," J. Mol. Spectrosc. **97**, 253 (1983).

[65]H. Partridge, S. R. Langhoff, C. W. Bauschlicher, Jr., and D. W. Schwenke, "Theoretical study of the $A'\ ^5\Sigma_g^+$ and $C'\ ^5\Pi_u$ states of N_2: Implications for the N_2 afterglow," J. Chem. Phys. **88**, 3174 (1988).

[66]R. M. Fristrom and A. A. Westenberg, *Flame Structure* (McGraw-Hill, New York, 1965).

[67]M. Capitelli, U. T. Lamanna, C. Guidotti, and G. P. Arrighini, "Comment on 'Spin-polarized atomic nitrogen and the $^7\Sigma_u^+$ state of N_2," J. Chem. Phys. **79**, 5210 (1983).